Supplementary Information

Theoretical prediction by DFT and experimental observation of heterocation-doping effects on hydrogen adsorption and migration over CeO$_2$ (111) surface

Kota Murakami[1], Yuta Mizutani[1], Hiroshi Sampei[1], Atsushi Ishikawa[2], Yuta Tanaka[1], Sasuga Hayashi[1], Sae Doi[1], Takuma Higo[1], Hideaki Tsuneki[1], Hiromi Nakai[3], Yasushi Sekine[1]

[1] Applied Chemistry, Waseda University, 3-4-1, Okubo, Shinjuku, Tokyo 169-8555, Japan

[2] National Institute for Materials Science, 1-1, Namiki, Tsukuba, Ibaraki 305-0044, Japan

[3] Chemistry and Biochemistry, Waseda University, 3-4-1, Okubo, Shinjuku, Tokyo 169-8555, Japan

1. Oxygen vacancy formation energy

Oxygen vacancy formation energies ($E(\text{O}_{\text{vac}})$) are calculated for considering the charge compensation. $E(\text{O}_{\text{vac}})$ is expressed as shown in below.

$$E(\text{O}_{\text{vac}}) = \frac{E(\text{slab with } n \text{ O}_{\text{vac}}) - E(\text{slab without O}_{\text{vac}}) - n/2\, E(\text{molecular O}_2)}{n} \quad (\text{s1})$$

E(slab with/without n O$_{\text{vac}}$) denotes the total energy of the slab with/without oxygen vacancy. The "n" means amount of oxygen vacancy. E(molecular O$_2$) represents the total energy of gaseous O$_2$. Gaseous O$_2$ was placed in a $10 \times 10 \times 10$ Å cubic box. Calculations were performed at Γ point. The obtained values are summarized in Table S3. Results indicated that the charge difference was compensated by oxygen vacancies (except for Al).

2. Bader charge analysis of lattice oxygen

We performed Bader charge analysis [s1-s4] for considering the dopant influence on electronic

state of surface O_{lat} using 'Fix surface' and 'Relax surface'. Heterocation-doping effects vary greatly between the oxygen next to the dopant and the other oxygen [s5]. Hence, the calculated Bader charges were classified into the charges of surface O_{lat} coordinated to Ce solely (Fig. S5) and that of surface O_{lat} coordinated to dopant (Fig. S6). Regarding surface O_{lat} coordinated to Ce solely, lower valence cation doping led to the substantial decrease in Bader charge of oxygen over 'Fix surface', meaning the formation of Lewis acid sites (Fig. S5(a)). The effect becomes more pronounced as the ionic radius of the heterocations increases. This is due to the high dispersion of cations with large ionic radii. However, some of those Lewis acid sites regained electron during lattice relaxation (Fig. S5(b)). The charge difference between 'Relax surface' and 'Fix surface' is summarized in Fig. S5(c). The charge transfer was significant over larger cations doped surfaces. It is true because large cation doping cause shrinkage of surrounding Ce-O bond as summarized in Fig. S4. In terms of O_{lat} coordinated to dopant (Fig. S6), Al, Ga, and Y doped surfaces showed much different trend from that of O_{lat} coordinated to Ce solely. It indicates the adjoining of two dopants induced significant change of electronic states. When the ionic radius of the doped cation is remarkably small, the coordination status of oxygen around the dopant changes significantly between the 'Fix surface' and the 'Relax surface' as shown in Fig. S3. This causes pronounced electronic transitions (Fig. S6(c)). The calculated Bader charges of all surface O_{lat} were summarized in Fig. S7. Moreover, Figures S8-S10 visually portray the change in surface oxygen Bader charge caused by heterocation-doping. Outermost O_{lat} was described as balls solely. The yellow triangles in Figures denote the planes passing through lattice oxygen and cations. The balls were colored along with the difference of Bader charge by doping. The charge over pristine CeO_2 was set to the reference value. Blue sites represent the electron deficient oxygen, and red sites denote the electron rich oxygen. Additionally, for increasing the color contrast, the color scale limit was set to ± 0.1 e. Results suggested the key influence of dopant distribution. Visually, adjoining of two dopants induced significant change of

2

electronic states even after lattice relaxation.

3. Reducible cation doping effects

The role of reducibility of heterocations was investigated using Ti as a model. All calculations were conducted in the similar way as we conducted for other dopants. Figure S11 shows the obtained surface ('Relax surface'). The obtained energies were inserted in Fig. 3 for comparison with other cations, see Fig. S12. As a result, Ti doping greatly enhanced H atom adsorption. Especially, strongest adsorption of H atom was confirmed over Ti doped surface as for 'Fix2 adsorption'. Ti^{4+} prone to be reduced into Ti^{3+} easily. Thus, we assumed that Ti^{4+} served as an electron reservoir to promote adsorption of H atom.

4. XRD measurements

XRD patterns of CeO_2 and $Ce_{0.9}M_{0.1}O_{2-\delta}$ (M: Sr, Al, Y, Zr) are summarized in Fig. S13. The obtained spectrums were almost identical among all samples, though slight peak shifts were confirmed. Therefore, we concluded that heterocation-doped samples kept the basic matrix of fluorite CeO_2.

5. X-ray photoelectron spectroscopy (XPS)

XPS measurements were performed using Versa Probe II (Ulvac-Phi inc.). The obtained C1s and O1s spectrum are shown in Fig. S14-S15.

6. Activity tests

NH_3 synthesis rate in the electric field was measured using $5wt\%Fe/CeO_2$ and $5w\%Fe/Ce_{0.9}M_{0.1}O_{2-\delta}$ (M: Sr, Al, Y, Zr). Details of the obtained data are summarized in Table S4.
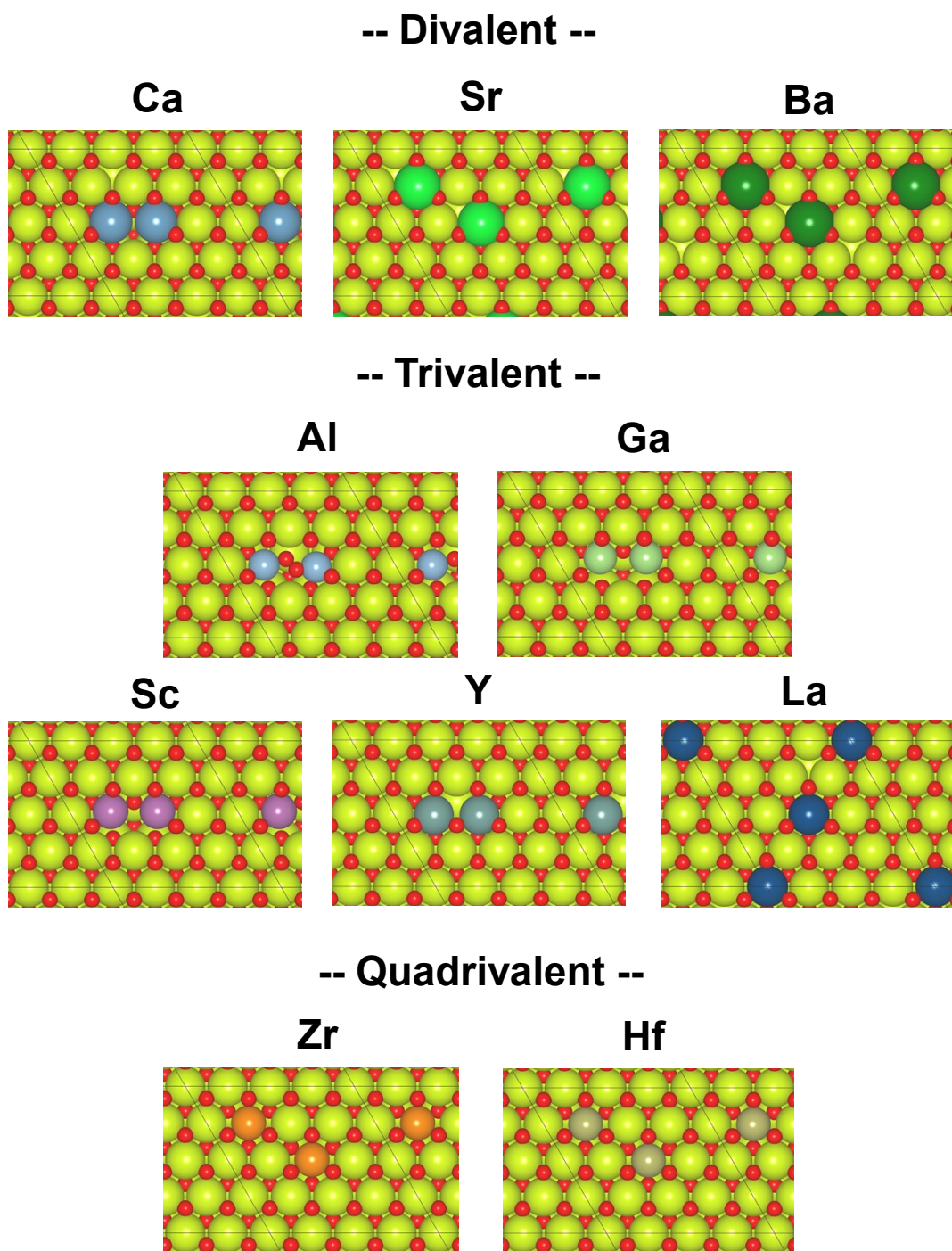
7. Characterization

Fe particle size after reduction under harsh condition (773 K for 1 h under $N_2 : H_2 = 1 : 3$ with 240 SCCM total flow) was measured using a field emission transmission electron microscope (FE-TEM; HF-2200; Hitachi Ltd.) with an energy-dispersive X-ray spectrometer (EDX). The obtained mean Fe particle size is shown in Table S5.

-- Divalent --

Ca   Sr   Ba

-- Trivalent --

Al   Ga

Sc   Y   La

-- Quadrivalent --

Zr   Hf   Ce
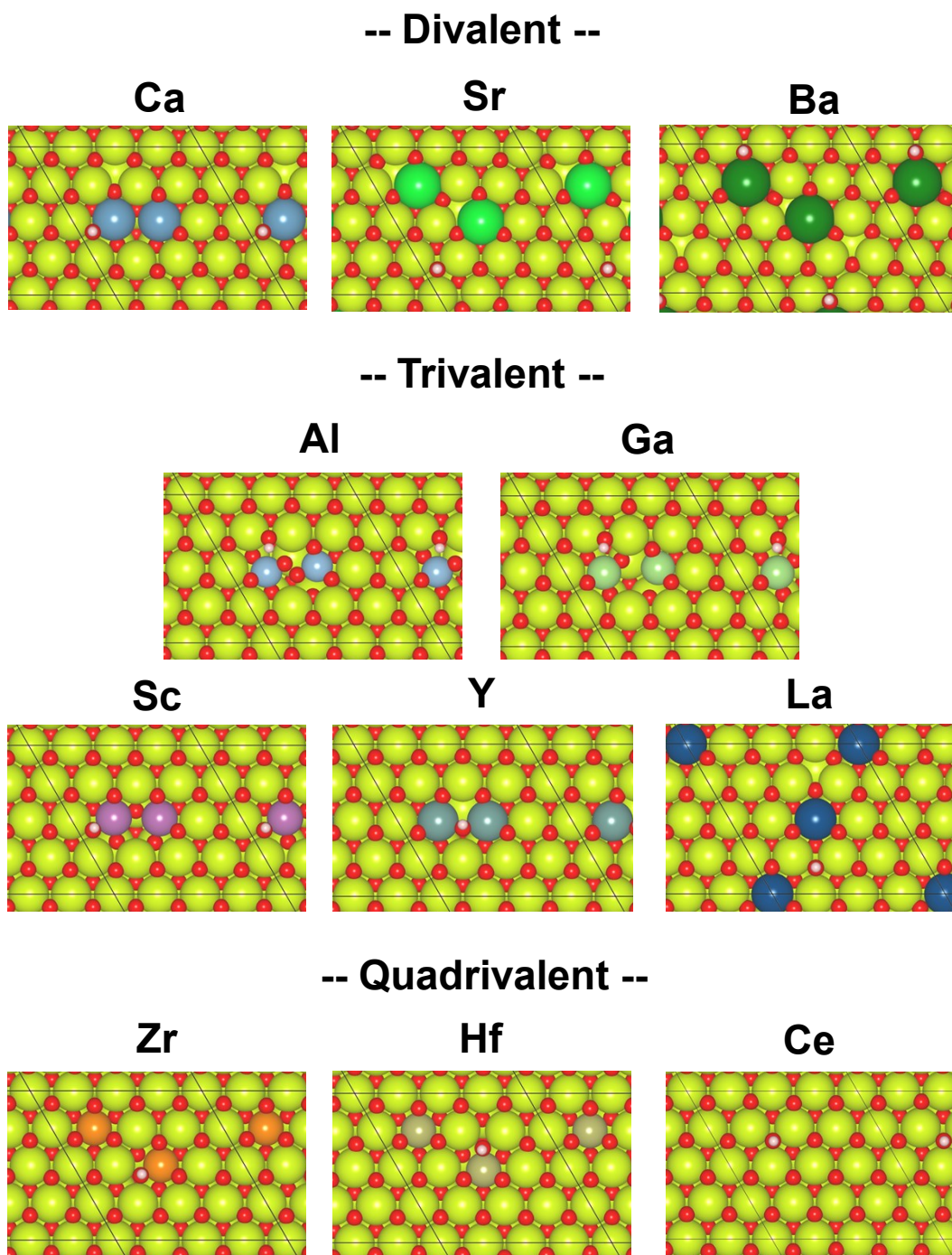
Fig. S1. Top view of the DFT–optimized heterocation-doped CeO_2 (111) surface with H atom ('Relax adsorption' in Fig. 1). Yellow denotes Ce. Red is oxygen. Small pink ball stands for H. Others represent dopants.

Electrode

Inlet gas

Power supplying device

Catalyst bed

Thermocouple

Outlet gas
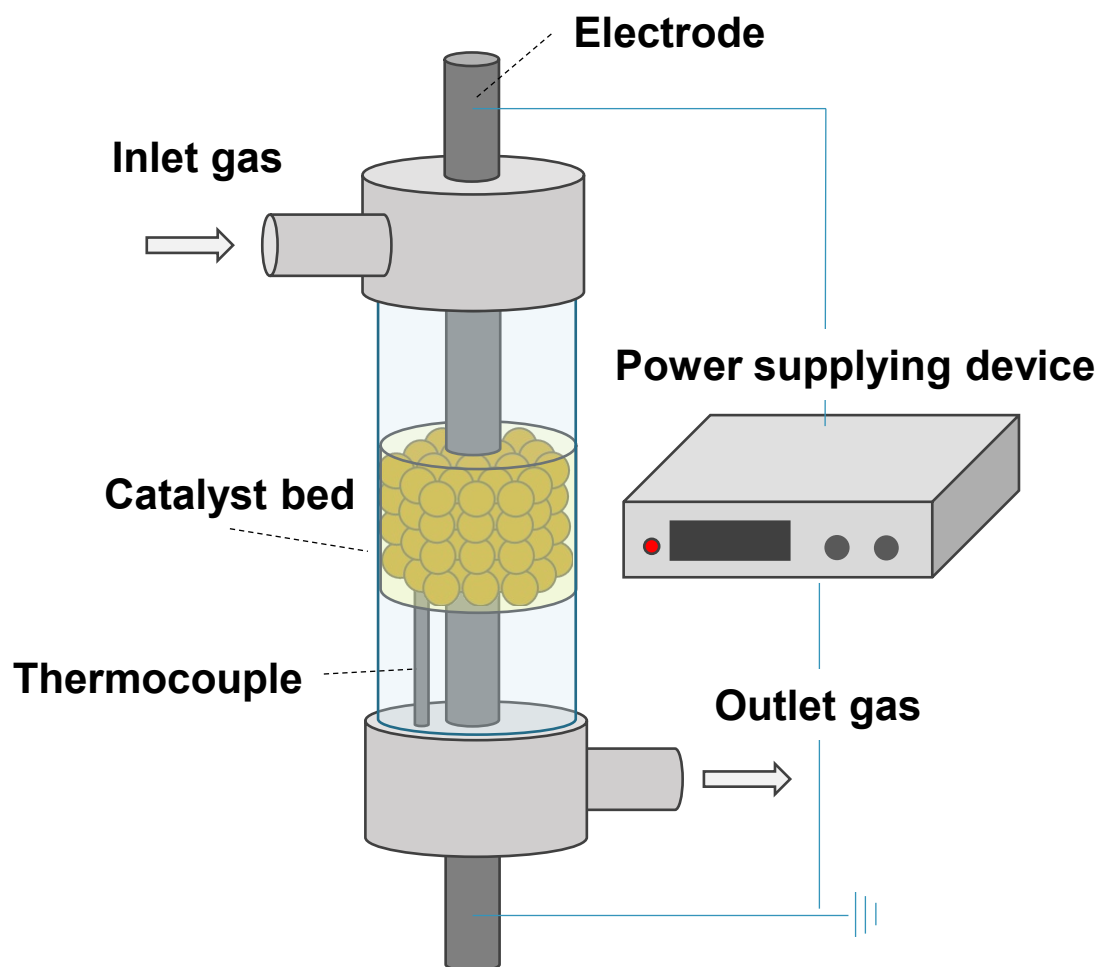
Fig. S2. Schematic image of the reactor.

-- Divalent --

Ca

Sr

Ba

-- Trivalent --

Al

Ga

Sc

Y

La

-- Quadrivalent --

Zr

Hf

Fig. S3. Top view of the DFT–optimized heterocation-doped CeO$_2$ (111) surface with oxygen vacancy for charge compensation ('Fix surface' in Fig. 1). Yellow denotes Ce. Red is oxygen. Others represent dopants.
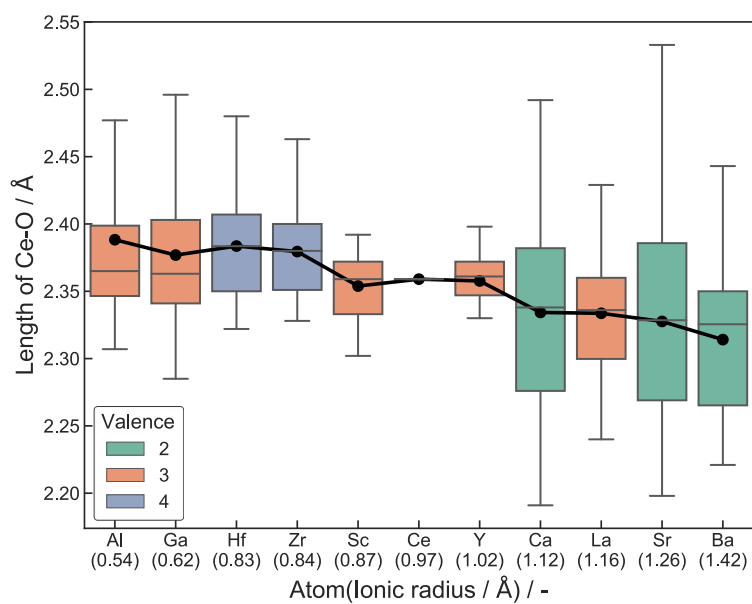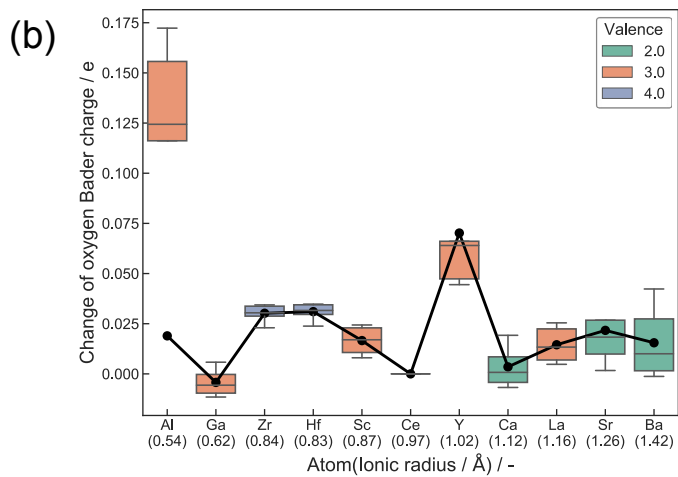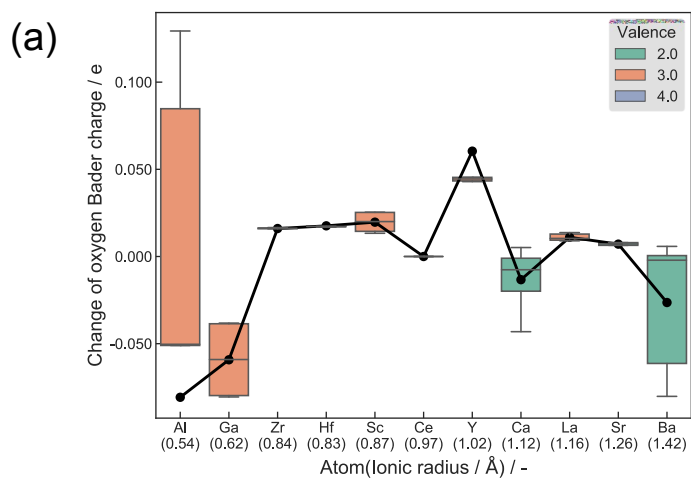
Fig. S4. Box plots for the length of Ce-O at the top O-Ce-O layer. The whisker length is set as 1.5 times of interquartile range. Black plots show average values.
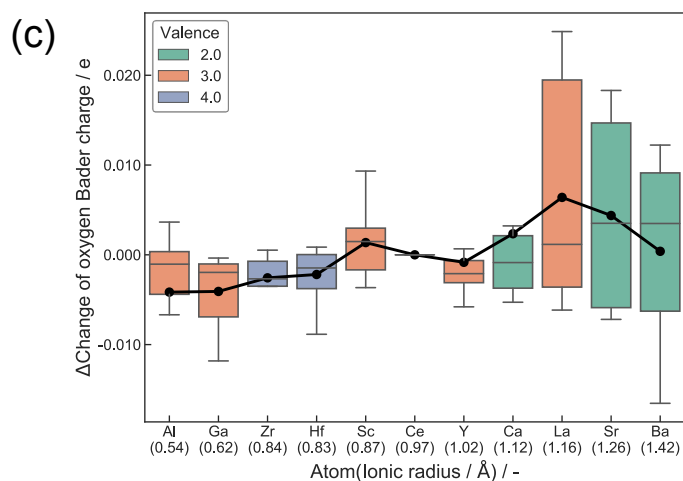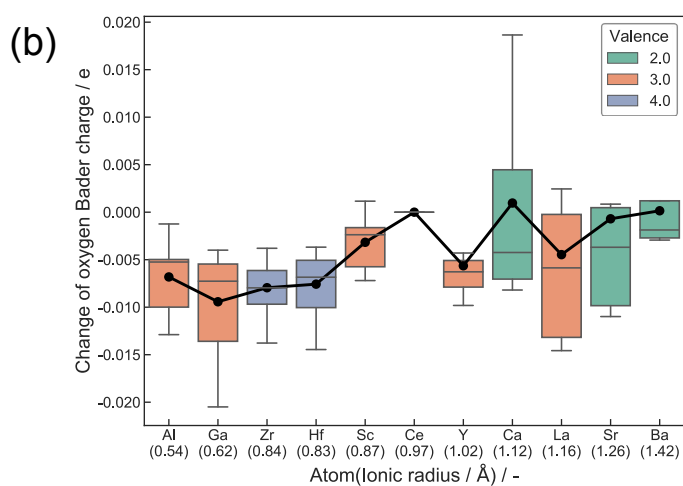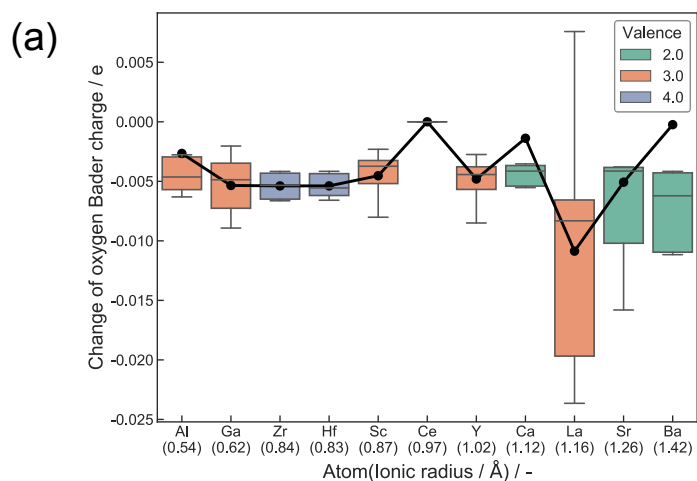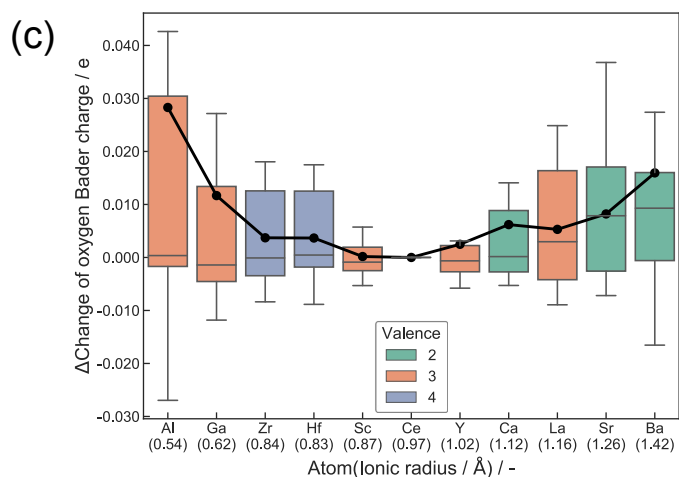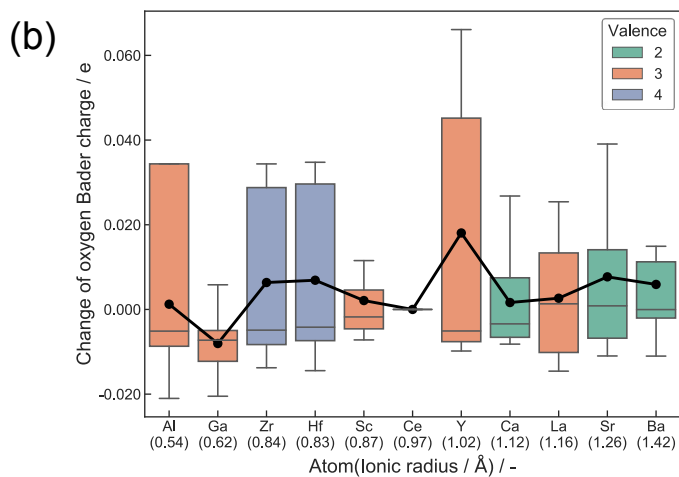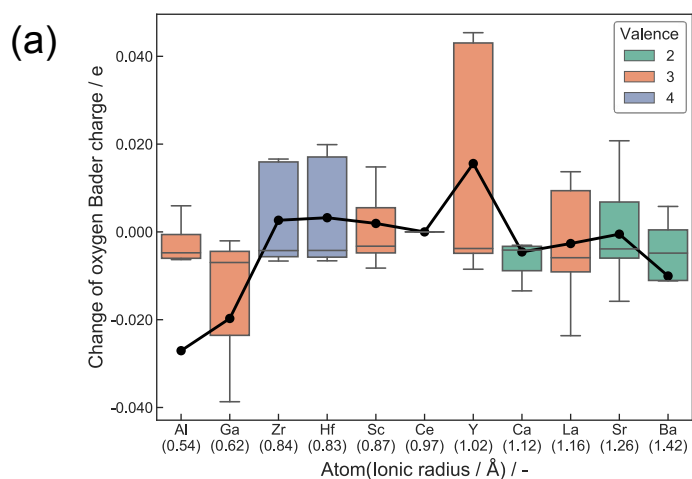
Fig. S5. Box plots for the difference in Bader charge of surface O_{lat} coordinated to Ce solely using CeO_2 (111) as a reference. (a) 'Fix surface', (b) 'Relax surface', and (c) difference between 'Relax surface' and 'Fix surface'. The whisker length is set as 1.5 times of interquartile range. Black plots show average values.

9
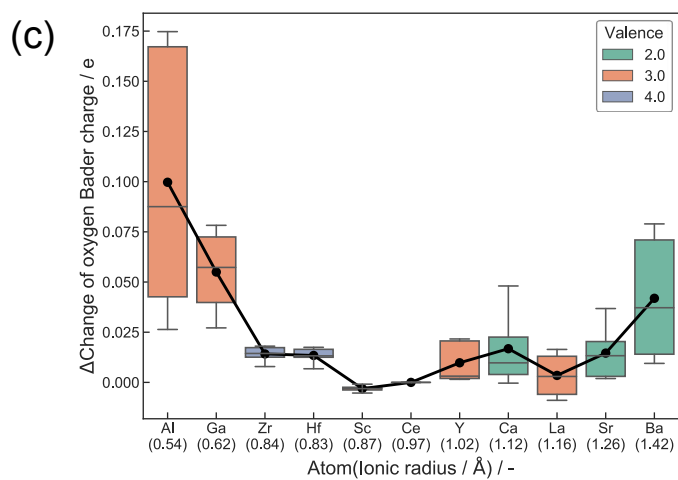
Fig. S6. Box plots for the difference in Bader charge of surface O_{lat} coordinated to dopants using CeO_2 (111) as a reference. (a) 'Fix surface', (b) 'Relax surface', and (c) difference between 'Relax surface' and 'Fix surface'. The whisker length is set as 1.5 times of interquartile range. Black plots show average values.

Fig. S7. Box plots for the difference in Bader charge of all surface O_{lat} using CeO_2 (111) as a reference. (a) 'Fix surface', (b) 'Relax surface', and (c) difference between 'Relax surface' and 'Fix surface'. The whisker length is set as 1.5 times of interquartile range. Black plots show average values.
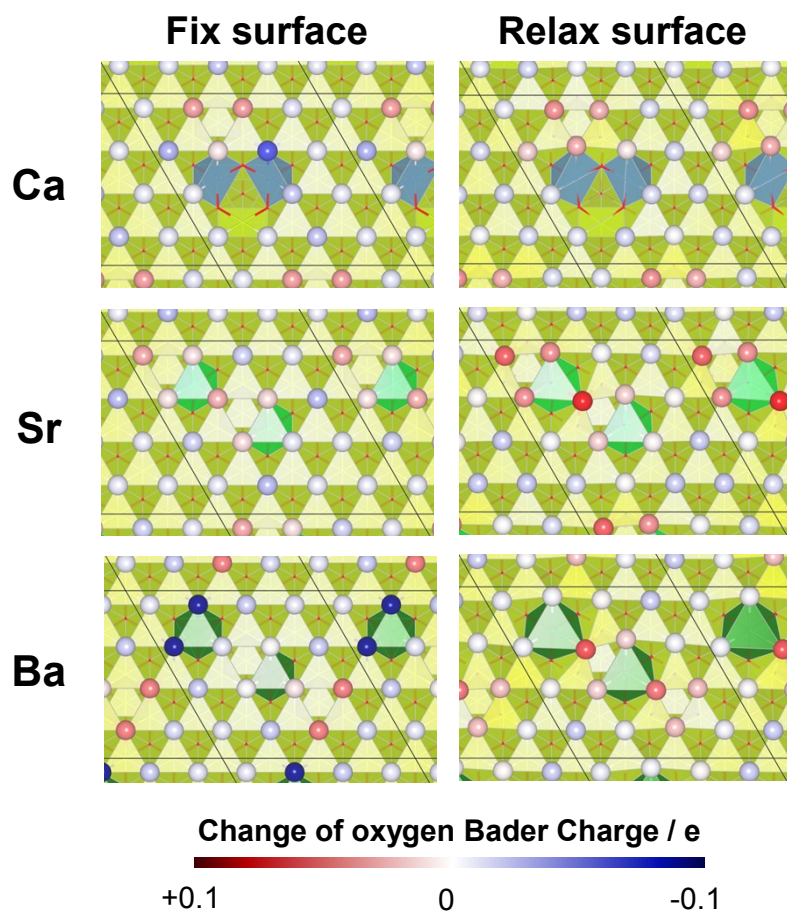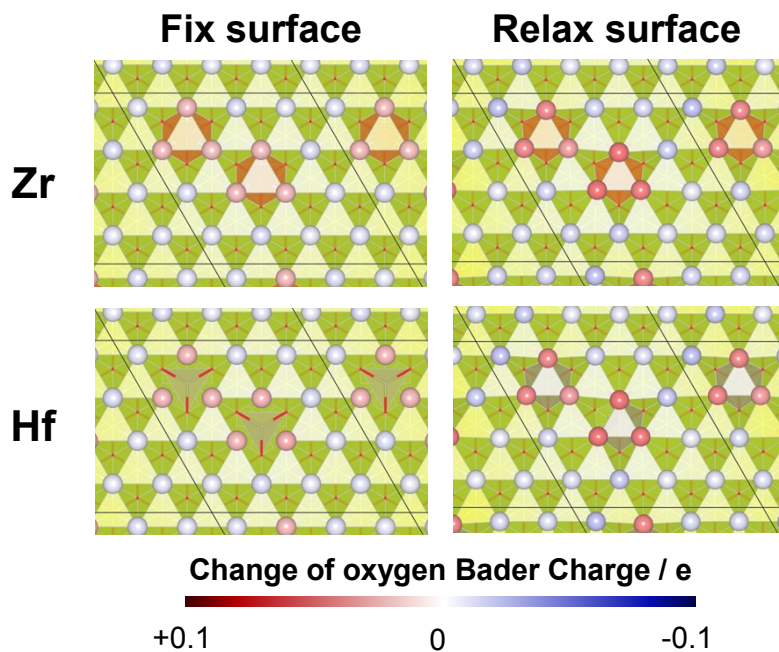
Fig. S8. Color maps for oxygen Bader charge difference over divalent cation doped models using CeO$_2$ (111) as a reference. Left side is 'Fix surface', and right side is 'Relax surface'. Red balls show the electron rich oxygen, and blue balls conversely mean the electron deficient one.
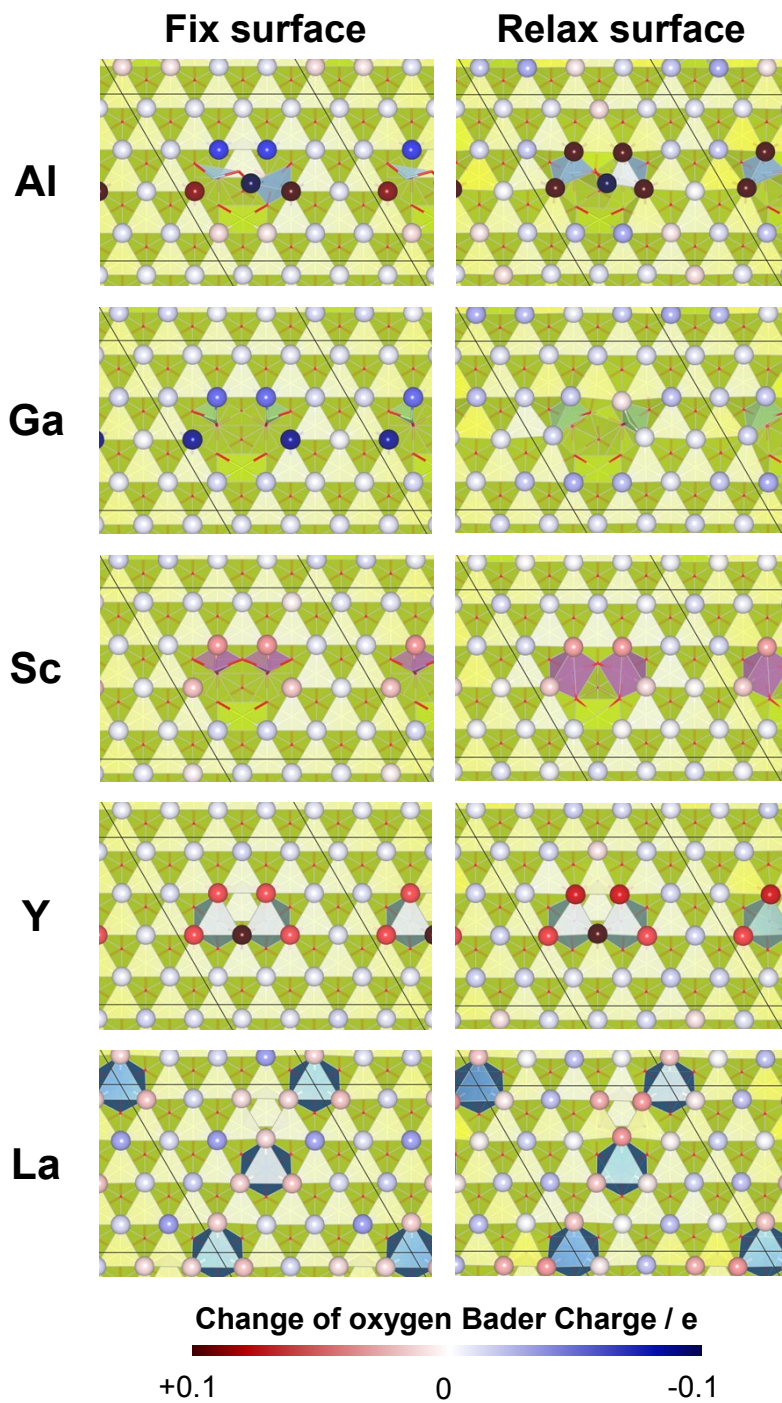
Fig. S9. Color maps for oxygen Bader charge difference over trivalent cation doped models using CeO$_2$ (111) as a reference. Left side is 'Fix surface', and right side is 'Relax surface'. Red balls show the electron rich oxygen, and blue balls conversely mean the electron deficient one.
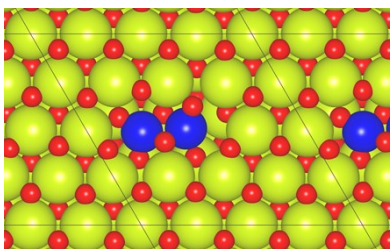
Fig. S10. Color maps for oxygen Bader charge difference over quadrivalent cation doped models using CeO_2 (111) as a reference. Left side is 'Fix surface', and right side is 'Relax surface'. Red balls show the electron rich oxygen, and blue balls conversely mean the electron deficient one.
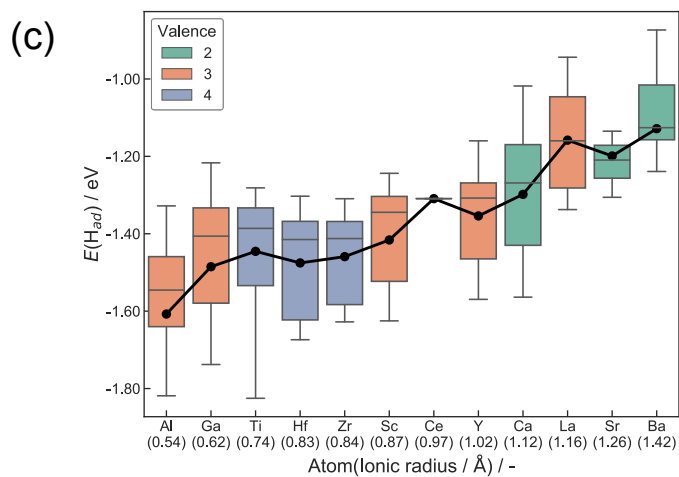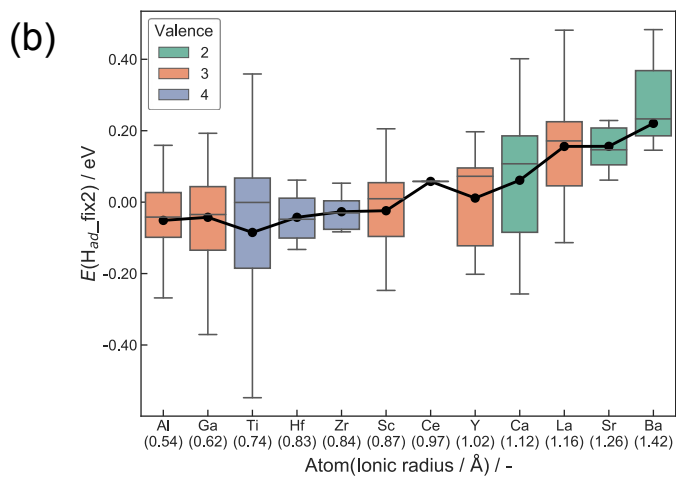

Fig. S11. Top view of the DFT-optimized Ti doped CeO_2 (111). Yellow denotes Ce, red is Oxygen, and blue is Ti.
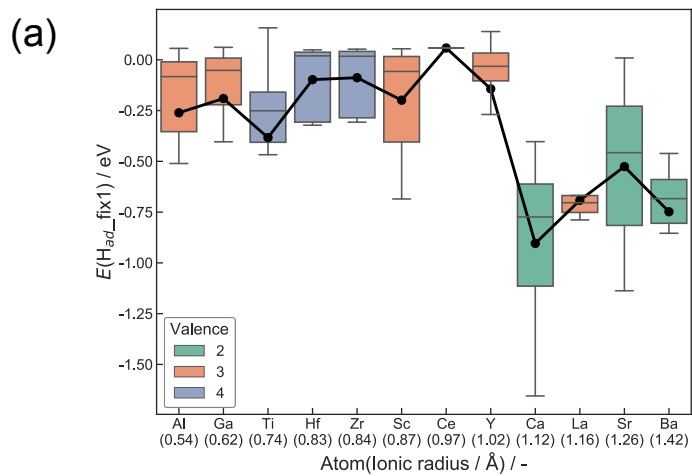
Fig. S12. Box plots for H adsorption energies containing data of Ti doped surface. (a) 'Fix1 adsorption', (b) 'Fix2 adsorption' and (c) 'Relax adsorption'. The whisker length is set as 1.5 times of interquartile range. Black plots show average values.
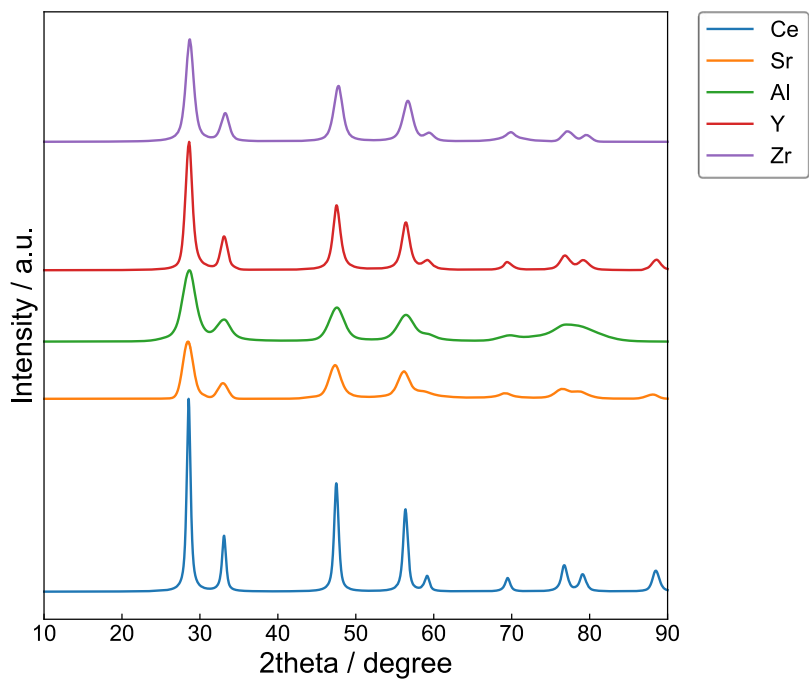
Fig. S13. XRD patterns of CeO$_2$ an Ce$_{0.9}$M$_{0.1}$O$_{2-\delta}$ (M : Sr, Al, Y, and Zr). The legends describe dopants (M), and Ce means spectrum of CeO$_2$.
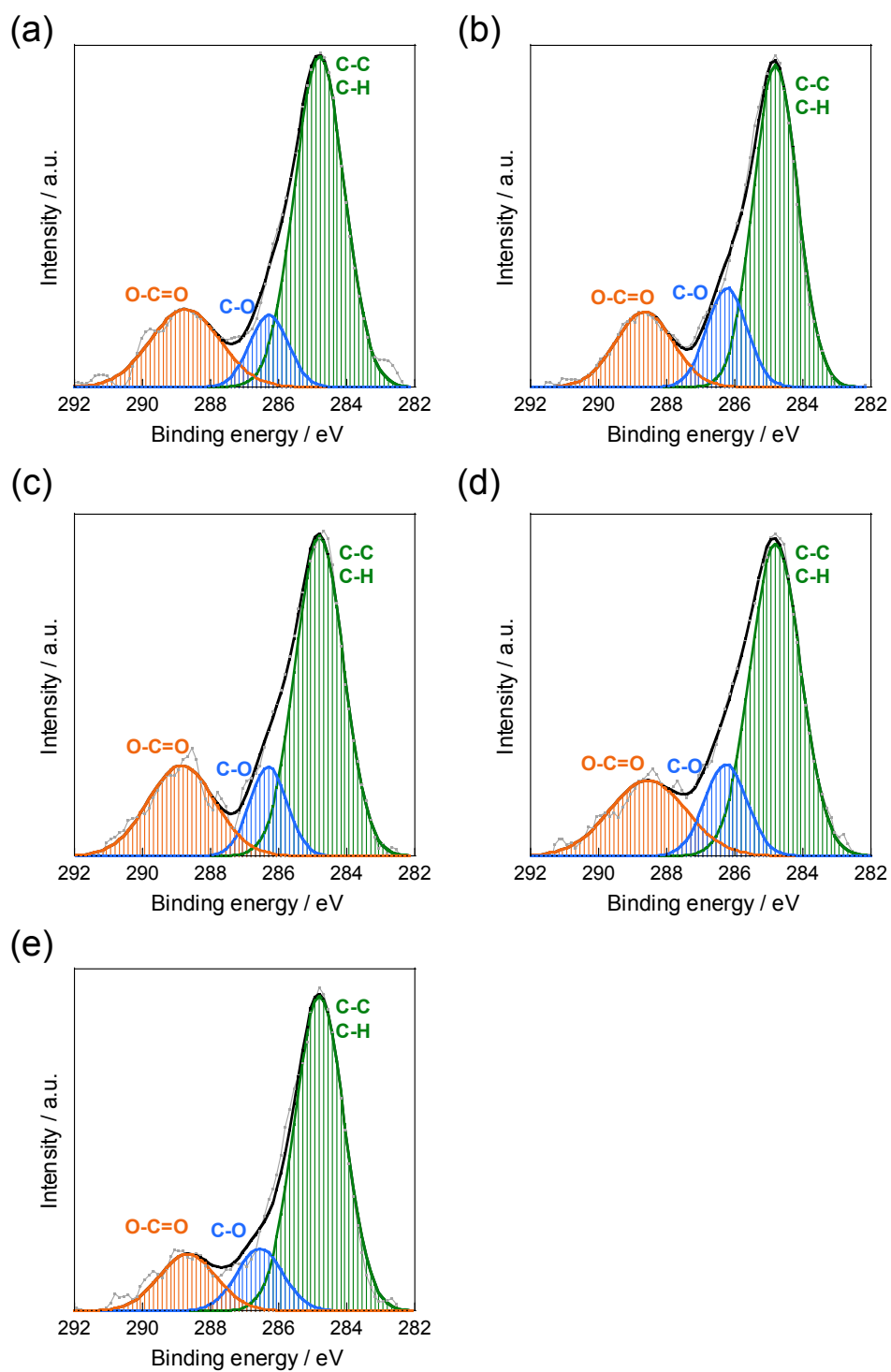
Fig. S14. C 1*s* X-ray photoelectron spectra after pre-reduction at 773 K for 1 h.: (a) CeO_2, (b)$Ce_{0.9}Sr_{0.1}O_{2-\delta}$, (c)$Ce_{0.9}Al_{0.1}O_{2-\delta}$, (d)$Ce_{0.9}Y_{0.1}O_{2-\delta}$, (e)$Ce_{0.9}Zr_{0.1}O_2$.
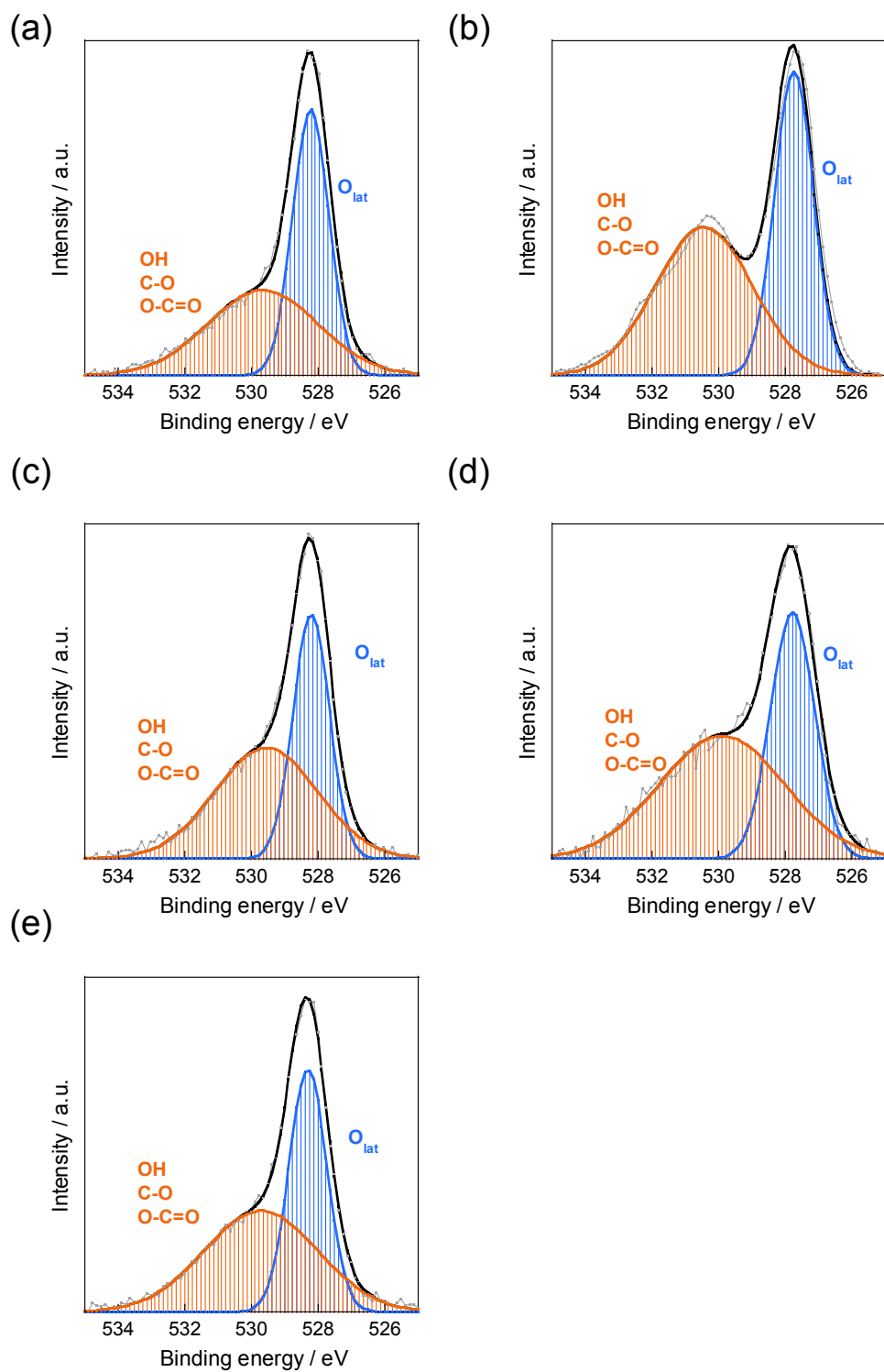
Fig. S15. O 1s X-ray photoelectron spectra after pre-reduction at 773 K for 1 h.: (a) CeO$_2$, (b)Ce$_{0.9}$Sr$_{0.1}$O$_{2-\delta}$, (c)Ce$_{0.9}$Al$_{0.1}$O$_{2-\delta}$, (d)Ce$_{0.9}$Y$_{0.1}$O$_{2-\delta}$, (e)Ce$_{0.9}$Zr$_{0.1}$O$_2$.

Table S1. Valence configurations used for DFT calculations.

Atom	Valence configuration
/-	/ -
Ca	$4s^2$
Sr	$5s^2$
Ba	$6s^2$
Al	$3s^23p^1$
Ga	$3d^{10}4s^24p^1$
Sc	$3d^14s^2$
Y	$4d^15s^2$
La	$5s^25p^65d^16s^2$
Ti	$3d^24s^2$
Zr	$4s^24p^64d^25s^2$
Hf	$5p^65d^26s^2$
Ce	$4f^15s^25p^65d^16s^2$
O	$1s^22s^22p^5$
H	$1s^1$

Table S2. Precursors used for supports synthesis.

Cation	Precursor
/ -	/ -
Sr	$Sr(NO_3)_2$
Al	$Al(NO_3)_3 \cdot 9H_2O$
Y	$Y(NO_3)_3 \cdot 6H_2O$
Zr	$ZrO(NO_3)_2 \cdot 2H_2O$
Ce	$Ce(NO_3)_3 \cdot 6H_2O$

Table S3. Oxygen vacancy formation energies $E(O_{vac})$. "n" denotes the amount of oxygen vacancies.

Dopant	n	$E(O_{vac})$
/ -	/ -	/ eV
Pristine	1	2.98
Ca	1	-0.80
	2	-1.41
	3	0.83
Sr	1	-0.66
	2	-1.23
	3	1.25
Ba	1	-0.71
	2	-0.61
	3	2.49
Al	1	0.59
Ga	1	-0.63
	2	0.08
Sc	1	-0.95
	2	0.76
Y	1	-0.72
	2	2.36
La	1	-0.67
	2	2.59
Ti	1	0.42
Zr	1	1.92
Hf	1	1.68

Table S4. Results of activity tests with the electric field over $5wt\%Fe/CeO_2$ and $5wt\%Fe/Ce_{0.9}M_{0.1}O_{2-\delta}$ (M: Sr, Al, Y, Zr, and Y).

Dopant	Imposed current	Response voltage	Catalyst bed temperature	NH$_3$ synthesis rate per power	TOF-p per power
/ -	/ mA	/ kV	/ K	/ μmol g^{-1} h^{-1} W^{-1}	/ s^{-1} W^{-1}
Ce		-0.22	377	171	0.18
		-0.24	380	148	0.16
		-0.20	401	100	0.11
		-0.14	405	96	0.10
Al		-0.33	415	146	0.09
		-0.39	421	120	0.07
Zr		-0.29	393	163	0.15
		-0.29	415	164	0.13
		-0.31	417	148	0.12
	6	-0.39	421	132	0.17
		-0.30	447	186	0.13
Y		-0.26	381	132	0.14
		-0.26	375	129	0.14
		-0.23	405	136	0.15
		-0.24	406	136	0.15
		-0.24	423	142	0.15
		-0.22	431	158	0.17
Sr		-0.24	389	110	0.13
		-0.29	403	103	0.12
		-0.22	411	133	0.16

Table S5. Mean Fe particle size over 5wt%Fe/CeO$_2$ and 5wt%Fe/Ce$_{0.9}$M$_{0.1}$O$_{2-\delta}$ (M: Sr, Al, Y, Zr, and Y).

Catalyst / -	Mean Fe particle size / nm
5wt%Fe/CeO$_2$	29
5wt%Fe/Ce$_{0.9}$Sr$_{0.1}$O$_{2-\delta}$	31
5wt%Fe/Ce$_{0.9}$Al$_{0.1}$O$_{2-\delta}$	22
5wt%Fe/Ce$_{0.9}$Y$_{0.1}$O$_{2-\delta}$	30
5wt%Fe/Ce$_{0.9}$Zr$_{0.1}$O$_{2-\delta}$	27

Reference

[s1] W. Tang, E. Sanville and G. Hnkelman, *J. Phys. Condes. Matter.*, 2009, **21**, 084204.

[s2] E. Sanville, S. D. Kenny, R. Smith and G. Henkelman, *J. Comp. Chem.*, 2007, **28**, 899-908.

[s3] G. Henkelman, A. Arnaldsson and H. Jónsson, *Comut. Mater. Sci.*, 2006, **36**, 354-360.

[s4] M. Yu and D. R. Trinkle, *J. Chem. Phys.*, 2011, **134**, 064111.

[s5] K. Murakami, S. Ogo, A. Ishikawa, Y. Takeno, T. Higo, H. Tsuneki, H. Nakai and Y. Sekine, *J. Chem. Phys.*, 2020, **152**, 014707.